nanomaterials

MDPI

Article

The Design of the Ni_3N/Nb_4N_5 Heterostructure as Bifunctional Adsorption/Electrocatalytic Materials for Lithium–Sulfur Batteries

Xialei Li [1], Wen Shang [1], Shan Zhang [1,2], Chun Xu [1], Jiabiao Lian [2] and Guochun Li [1,2,3,*]

[1] Key Laboratory of Fine Chemical Application Technology of Luzhou, Sichuan Vocational College of Chemical Technology, Luzhou 646300, China; zhangshan@sccc.edu.cn (S.Z.)
[2] Key Laboratory of High-Tech Research on Power Batteries and Energy Storage of Zhenjiang, Institute for Energy Research, Jiangsu University, Zhenjiang 212013, China; jblian@ujs.edu.cn
[3] Huizhou Research Institute, Sun Yat-sen University, Huizhou 516081, China
* Correspondence: liguochun@ujs.edu.cn

Abstract

Lithium–sulfur (Li-S) batteries are hindered by the sluggish electrochemical kinetics and poor reversibility of lithium polysulfides (LiPSs), which limits their practical energy density and cycle life. In order to address this issue, a novel Ni_3N/Nb_4N_5 heterostructure was synthesized via electrospinning and nitridation as a functional coating for polypropylene (PP) separators. Adsorption experiments were conducted in order to ascertain the heterostructure's superior affinity for LiPSs, thereby effectively mitigating their shuttling. Studies of Li_2S nucleation demonstrated the catalytic role of the substance in accelerating the deposition kinetics of Li_2S. Consequently, Li-S cells that employed the Ni_3N/Nb_4N_5-modified separator were found to achieve significantly enhanced electrochemical performance, with the cells delivering an initial discharge capacity of 1294.4 mAh g^{-1} at 0.2 C. The results demonstrate that, after 150 cycles, the cells retained a discharge capacity of 796.2 mAh g^{-1}, corresponding to a low capacity decay rate of only 0.25% per cycle. In addition, the rate capability of the cells was found to be improved in comparison to control cells with $NiNb_2O_6$-modified or pristine separators.

Keywords: lithium–sulfur batteries; heterostructure; modified separator; adsorption; electrocatalysis

check for updates

Academic Editor: Carlos Miguel Costa

Received: 15 May 2025
Revised: 16 June 2025
Accepted: 20 June 2025
Published: 1 July 2025

Citation: Li, X.; Shang, W.; Zhang, S.; Xu, C.; Lian, J.; Li, G. The Design of the Ni_3N/Nb_4N_5 Heterostructure as Bifunctional Adsorption/Electrocatalytic Materials for Lithium–Sulfur Batteries. *Nanomaterials* **2025**, *15*, 1015. https://doi.org/10.3390/nano15131015

Copyright: © 2025 by the authors. Licensee MDPI, Basel, Switzerland. This article is an open access article distributed under the terms and conditions of the Creative Commons Attribution (CC BY) license (https://creativecommons.org/licenses/by/4.0/).

1. Introduction

The pursuit of high-energy-density, sustainable energy storage technologies has prompted extensive research into metal–air batteries (MABs) and lithium–sulfur (Li-S) batteries as promising alternatives to conventional lithium-ion batteries (LIBs). Although theoretical analyses indicate that MABs, including lithium–air (Li-air) and sodium–air (Na-air) systems, possess the potential to exhibit exceptional energy densities, their practical deployment remains constrained by critical challenges [1–4].

In contrast, Li-S batteries offer a compelling balance of theoretical energy density (2600 Wh/kg, six times higher than lithium-ion (Li-ion) batteries), material abundance (sulfur is inexpensive and abundant in the earth's crust), and environmental benignity [5,6]. However, several critical challenges remain unresolved. Among these, the design of sulfur-containing host materials has been demonstrated as an effective strategy to enhance cycling stability, as evidenced by extensive studies [7–10]. Numerous host materials, such as

metal oxides [11,12], sulfides [13], and nitrides [14–16], as well as metallic species with distinct dispersion states (e.g., nanoparticles [17–19] and single-atom catalysts [20,21]), have exhibited catalytic effects in facilitating the rapid and efficient conversion of long-chain lithium polysulfide to Li_2S. It is well known that the size of the electrocatalyst significantly affects its catalytic activity in non-homogeneous catalysis, there is no theory to explain and predict the behavior of electrocatalysts with different particle sizes in different reactions, and the dependence of the kinetics of sulfur redox electrocatalysis on the degree of aggregation of the electrocatalyst atoms is yet to be explored [22], which is also crucial for understanding the underlying basis of electrocatalysis in Li-S batteries.

Since Manthiram et al. introduced the concept of employing functional interlayers or coatings between the cathode and separator to suppress the polysulfide shuttle effect and enhance sulfur utilization in 2012 [23], significant efforts have been dedicated to developing advanced interlayer materials. Transition metal compounds [24–34] (e.g., oxides, nitrides, sulfides, and selenides) have emerged as promising candidates due to their strong polar-polar interactions with LiPSs and superior chemisorption capabilities [35], thereby effectively improving cell stability.

In some cases, materials with identical chemical compositions may exhibit significantly distinct charge transfer mechanisms or thermodynamic properties, primarily governed by particle size variations [23]. Electrodes composed of smaller particles generally demonstrate higher electrical conductivity, which is critical for minimizing ohmic losses during cycling [36]. Furthermore, reducing the particle size of electrode materials typically enhances capacity retention at elevated current rates. This phenomenon can be rationalized through Fick's first law of diffusion and stochastic process theory [37], where the diffusion length is expressed as $L \propto \sqrt{D \times t}$, with D representing the diffusion coefficient of charge carriers and t denoting the characteristic diffusion time. Decreasing the particle size effectively reduces the diffusion time required for lithium-ion intercalation into the electrode bulk, thereby improving charge–discharge kinetics.

In recent years, heterojunction engineering has emerged as a promising strategy for modulating the electronic structure of catalytic materials. This approach leverages the unique capability of heterojunctions to regulate band structures, accelerate charge transfer, and enhance catalytic conversion from LiPS (lithium polysulfides) to Li_2S. Table 1 lists some recent heterojunction applications of the interlayers in Li-S batteries. As seen, Li et al. [38] synthesized a WS_{2-x}/ZnS@C composite, where the constructed heterojunction not only facilitates charge transfer and ion diffusion but also improves reaction kinetics, thereby boosting overall electrochemical performance. Similarly, Li et al. [39] reported a Co_9S_8@MoS_2 heterojunction material with pronounced energy-level separation. The impurity energy levels within the bandgap of Co_9S_8 were optimized, which enhanced its metallic characteristics and electrical conductivity. Beyond electronic modulation, heterojunctions also contribute to suppressing the shuttle effect, strengthening interfacial interactions, and enabling synergistic functionalities. Zhou et al. [40] developed a TiO_2-TiN heterojunction as a dense and ultrathin separator coating, which effectively restricts LiPS shuttling even under high sulfur loading, enabling seamless LiPS capture–diffusion–conversion across interfaces. Ren et al. [41] engineered 2D/2D $Ti_3C_2T_x$/Ni-Co MOF heterojunction nanosheets coated on separators, achieving dual functions of shuttle suppression and synergistic adsorption–electrocatalysis. Yao et al. [42] integrated SnS (with strong adsorption and high conductivity) and ZnS (with superior catalytic activity) into a ZnS-SnS@NC heterojunction encapsulated by an N-doped carbon shell. This architecture exhibited enhanced lithiophilic and sulfiphilic properties, significantly suppressing the shuttle effect while improving sulfur utilization and cycle stability. Lei et al. [43] designed a MoS_2-MoO_3 heterojunction nanosheet that shortens Li^+/electron transport pathways. Its strong

donor–acceptor interactions enhance interfacial electrochemical reactions, while the built-in electric field accelerates charge transfer and LiPS conversion. Moreover, the synergistic interplay between MoO_3 and MoS_2 provides abundant adsorption/catalytic sites, further mitigating the shuttle effect and boosting sulfur utilization. Despite these advances, individual components in heterojunctions often struggle to integrate multiple advantages, such as abundant catalytic active sites, robust chemical adsorption, high conductivity, and rapid Li^+ diffusion. Theoretical insights suggest that rational heterojunction design could holistically unify these merits, paving the way for next-generation electrocatalytic systems with unprecedented performance [44].

Table 1. Some recent heterojunction applications for Li-S battery interlayers.

		Typology	Current Density	Number of Cycles	Capacity Decay Rate	Capacity/Retention Rate
1	Co_9S_8@MoS_2/CNF	interlayer	1.0 C	400	0.09%	[39]
2	TiO_2–TiN	interlayer	0.3 C	300	/	927 mAh g^{-1} [40]
3	$Ti_3C_2T_x$/Ni-Co MOF	modified separators	0.2 C	200	0.06%	1100 mAh g^{-1}/87.3% [41]
4	ZnS-SnS@NC	modified separators	4.0 C	2000	0.01%	632 mAh g^{-1}/74.9% [42]
5	MoS_2-MoO_3	modified separators	1.0 C	600	0.01%	92.00% [43]
6	This work	modified separators	0.2 C	200	0.25%	796.2 mAh g^{-1}

In this study, we investigated the catalytic and adsorption mechanisms of metal nitride heterostructure toward lithium polysulfides (LiPSs). The Ni_3N/Nb_4N_5 heterostructure exhibits a uniform dispersion and porous architecture, which facilitates ion transport and provides abundant active sites for LiPS conversion. The visualization of adsorption tests and X-ray photoelectron spectroscopy (XPS) analysis confirmed the strong chemisorption capability of Ni_3N/Nb_4N_5 toward LiPSs. Furthermore, the constructed heterogeneous interface facilitates accelerated charge transfer kinetics, while the synergistic catalytic effect between bimetallic nitrides promotes the homogeneous nucleation and growth of Li_2S. Electrochemical evaluations demonstrate that the Ni_3N/Nb_4N_5-PP-based cell achieved enhanced cycling stability and rate capability, delivering discharge capacities of 1403.6, 1032.4, 909.5, and 793.9 mAh g^{-1} at 0.1 C, 0.25 C, 0.5 C, and 1.0 C, respectively. Notably, the Li-S cell retained a discharge capacity of 796.2 mAh g^{-1} after 150 cycles at 0.2 C.

2. Experimental Procedures

2.1. Materials

Niobium oxalate hydrate: Alfa Aesar Chemical Company (Shanghai, China); N,N-dimethylformamide: Sinopharm Chemical Reagent Company (Shanghai, China); nickel acetate tetrahydrate: Sinopharm Chemical Reagent Company (Shanghai, China); peroxyacetyl nitrate: Aladdin ReagentCompany (Shanghai China); electrolyte: DuoDuo Chemical Reagent (Suzhou, China); polyvinylidene fluoride: Aldrich Chemical Company (Shanghai, China); N-methylpyrrolidone: Sigma Chemical Reagent Company (Shanghai, China).

2.2. Fabrication of Ni_3N/Nb_4N_5 Heterostructure

The fabrication of the Ni_3N/Nb_4N_5 heterostructure was achieved through a sequential process that entailed the combination of electrospinning and controlled thermal treatments. The synthesis protocol that was utilized is outlined as follows:

Precursor solution preparation: The formation of a homogeneous solution was achieved through the dissolution of 2 mmol of niobium oxalate hydrate ($C_{10}H_5NbO_{20}$) in 4 mL of DMF, under constant stirring at 60 °C. Subsequently, 1 mmol of nickel acetate tetrahydrate ($Ni(CH_3COO)_2{\cdot}4H_2O$) was added, and the mixture was stirred for a further 8 h.

Polymer matrix preparation: Concurrently, 1 g of polyacrylonitrile (PAN) was dissolved in 6 mL of DMF, with the solution being subjected to mechanical stirring at ambient temperature for a duration of 8 h.

Electrospinning process: The two solutions were thoroughly blended prior to processing through the electrospinning apparatus.

Thermal conversion: The electrospun fibers were then subjected to oxidative calcination at 800 °C (with a 5 °C/min ramp rate) for a duration of three hours in air, with the objective of producing the $NiNb_2O_6$ intermediate.

Nitridation: The final transformation was achieved by subjecting the $NiNb_2O_6$ precursor to ammoniating at 800 °C for 3 h (with a heating rate of 5 °C/min) under NH_3/Ar flow, thereby yielding the desired Ni_3N/Nb_4N_5 nanocomposite.

2.3. Preparation of Modified Separators

The electrode slurry was prepared by means of homogenously blending active materials (Ni_3N/Nb_4N_5 heterostructure or alternatively $NiNb_2O_6$), a conductive additive (Super P carbon black), and a polymeric binder (PVDF) in an 8:1:1 mass ratio through mechanical grinding. The subsequent addition of N-methyl-2-pyrrolidone (NMP) as a dispersion medium enabled uninterrupted magnetic stirring for a period of three hours, thereby achieving a well-dispersed slurry. The slurry was uniformly coated onto a polypropylene (PP, Celgard 2400) separator using a 200 μm coating blade with a coating machine. Subsequently, the modified separator was dried in a vacuum oven at 50 °C for 12 h. Finally, the separator was punched into 19 mm diameter disks, with an active material (Ni_3N/Nb_4N_5 or $NiNb_2O_6$) loading of 1.3–1.9 mg cm^{-2}. The Ni_3N/Nb_4N_5 and $NiNb_2O_6$ modified separators were abbreviated as Ni_3N/Nb_4N_5-PP and $NiNb_2O_6$-PP.

2.4. Visualized Adsorption of Polysulfides

This section will deal with the Li_2S_6 solution synthesis. The solvent system was initially prepared by combining 1,3-dioxolane (DOL) and dimethoxyethane (DME) at a volumetric ratio of 1:1. Subsequently, stoichiometric amounts of Li_2S and elemental sulfur (in a 1:5 molar ratio) were dissolved in the DOL/DME mixture. The reaction system was maintained at a temperature of 60 °C for a period of 24 h, with the protection of argon, thereby yielding a solution of Li_2S_6 at a concentration of 5 mmol L^{-1}. This solution was then diluted to a concentration of 2 mmol L^{-1}. For the adsorption tests, 5 mL aliquots of the diluted solution were separately mixed with 10 mg portions of Ni_3N/Nb_4N_5 and $NiNb_2O_6$ powders in an inert environment. The mixtures were maintained for a duration of 0~24 h to monitor their adsorption behavior, and images were captured at designated time intervals for further analysis.

2.5. Fabrication and Characterization of Symmetric Cells

The active material (Ni_3N/Nb_4N_5 or $NiNb_2O_6$), conductive carbon black, and PVDF binder were then homogenously mixed in ethanol with a weight ratio of 8:1:1 under ultrasonication for 30 min to form a uniform electrode slurry. The homogenized slurry was uniformly deposited onto 12 mm diameter carbon fiber paper (Toray TGP-H-060,Toray Investment Co., Ltd., Shanghai, China)) using a micropipette, followed by drying at 50 °C for 12 h in a vacuum oven.

A CR2025 coin cell was assembled using a polypropylene (Celgard-2400) separator and 50 μL of Li_2S_6 electrolyte. The electrolyte was formulated by dissolving 1.0 M Li_2S_6 and 1.0 M LiTFSI in a 1:1 (v/v) binary solvent system comprising DOL and DME. The present study investigates the electrochemical behavior of LiPSs. To this end, cyclic voltammetry (CV) measurements were performed on the symmetric cell at scan rates of 5 and 50 mV s^{-1}. The potential window was set between −0.8 and 0.8 V.

2.6. Experimental Procedure for Li_2S Nucleation Studies

The nucleation behavior was investigated using CR2025-type coin cells. Carbon paper substrates were coated with Ni_3N/Nb_4N_5 or $NiNb_2O_6$ active materials, achieving mass loadings between 1.0 and 1.3 mg cm^{-2}. Lithium foil acted as the counter electrode. In the context of the electrolyte system, the cathodic compartment was constituted of 0.25 M Li_2S_6 in conjunction with 1.0 M LiTFSI within a tetraethylene glycol dimethyl ether solvent, while the anodic compartment utilized a 1.0 M LiTFSI solution within an equivalent solvent. Precise 20 μL aliquots of each electrolyte solution were dispensed into their respective cell chambers. Electrochemical conditioning was initiated with a constant-current discharge at 2.06 V (0.112 mA). This was followed by a potentiostatic hold at 2.05 V, which was maintained until the current stabilized below 10^{-5} A. This process was found to promote Li_2S crystallization [45].

2.7. Material Characterization

The crystalline structure was characterized by X-ray diffraction (XRD) analysis performed on a Bruker D8 Advance diffractometer equipped with a Cu Kα radiation source (wavelength = 1.54056 Å). The morphology and microstructure of the samples were characterized by scanning electron microscopy (SEM, JSM-7800F) and transmission electron microscopy (TEM, FEI Talos F200X G2, FEI Czech Ltd., Hillsboro, OR, USA), both equipped with energy-dispersive spectroscopy (EDS). The chemical composition of the sample was investigated through the implementation of X-ray photoelectron spectroscopy (XPS) analysis.

2.8. Material Preparation and Electrochemical Characterization

The sulfur/acetylene black (S/AB) composite was fabricated through mechanical ball-milling of sublimed sulfur and AB (3:2 mass ratio) for 2 h, followed by thermal treatment in a sealed reactor at 155 °C for 12 h. This facilitated sulfur melting and subsequent homogeneous distribution. Subsequent to cooling to ambient temperature, cathode slurries were prepared by blending the composite with PVDF binder (9:1 mass ratio) in NMP solvent. The homogeneous mixture was applied to carbon-modified Al current collectors by doctor-blading, followed by vacuum drying at 50 °C for 12 h. The electrodes were punched into 12 mm diameter disks, with sulfur loadings ranging from 1.0 to 1.5 mg cm^{-2}. The assembly of coin cells was conducted within an Ar atmosphere glovebox, utilizing lithium metal anodes, prepared S/AB cathodes, and Ni_3N/Nb_4N_5-PP (or an alternative) separators. The electrolyte formulation consisted of 1.0 M LiTFSI and 2 wt% $LiNO_3$ in DME (1:1 v/v) solvent, with strict control of electrolyte volume at 30 μL per mg sulfur. Galvanostatic charge–discharge tests were performed on a LAND battery testing system within a voltage window of 1.7–2.8 V. Cyclic voltammetry (CV) was conducted at a scan rate of 0.1 mV s^{-1}, and electrochemical impedance spectroscopy (EIS) was performed over a frequency range of 0.01 Hz to 100 kHz.

3. Results and Discussion

Figure 1 illustrates the preparation process of the $NiNb_2O_6$ nanorods and the Ni_3N/Nb_4N_5 heterostructure. Initially, $NiNb_2O_6$ nanorods, composed of uniformly sized nanoparticles, were synthesized via the electrospinning method, demonstrating high ho-

mogeneity. Subsequently, the $NiNb_2O_6$ nanorods underwent nitridation treatment in an ammonia atmosphere to form the Ni_3N/Nb_4N_5 heterostructure. After nitridation, the nanorods exhibited a well-dispersed morphology, leading to the formation of homogeneous Ni_3N/Nb_4N_5 nanoparticles.



Figure 1. Schematic diagram of the preparation of Ni_3N/Nb_4N_5 heterostructure.

The crystal structure of the as-prepared $NiNb_2O_6$ and Ni_3N/Nb_4N_5 heterostructure were analyzed and verified by XRD. As shown in Figure 2a, several typical diffraction peaks in the XRD pattern of $NiNb_2O_6$ are in good agreement with the reference spectrum of $NiNb_2O_6$ nanorods (JCPDS No. 76-2354), confirming the successful synthesis of crystalline $NiNb_2O_6$. In addition, Figure 2b shows the XRD pattern of the Ni_3N/Nb_4N_5 heterostructure, where the major diffraction peaks correspond to Nb_4N_5 (JCPDS No. 74-0606) and Ni_3N (JCPDS No. 89-5144). The presence of non-impurity peaks indicates that the pure Ni_3N/Nb_4N_5 heterostructure was successfully synthesized through the nitridation of $NiNb_2O_6$.

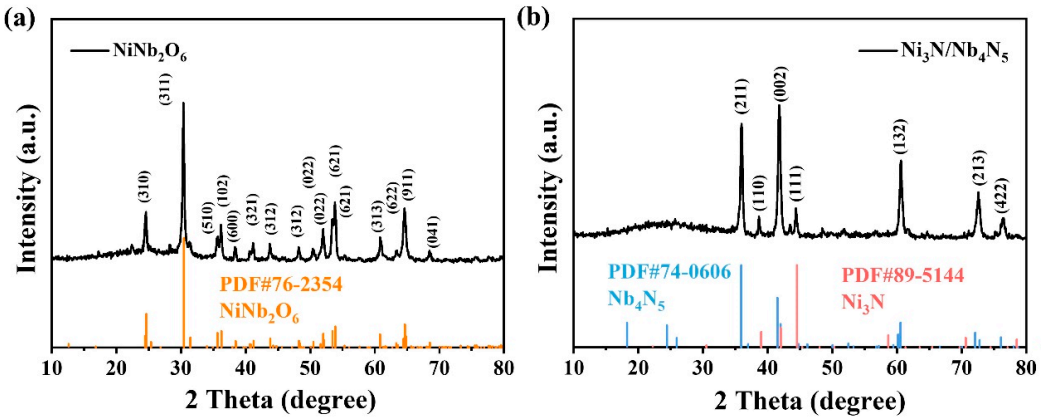


Figure 2. (**a**) XRD patterns of $NiNb_2O_6$ nanorods and (**b**) Ni_3N/Nb_4N_5 heterostructure.

The microstructure of $NiNb_2O_6$ and Ni_3N/Nb_4N_5 heterostructure, as well as the cross-section of the modified separator, were observed using scanning electron microscopy (SEM). As shown in Figure 3a, the $NiNb_2O_6$ exhibits a regular nanorod structure. In contrast, the nitrided Ni_3N/Nb_4N_5 heterostructure primarily displays a nanoparticle structure (Figure 3b), with uniform dispersion and good homogeneity. Moreover, the nanoparticle stacking structure features a large surface area, allowing the space between nanoparticles to be effectively infiltrated and stored with electrolyte, thereby enhancing the electron

exchange rate [46]. A slurry was prepared to coat the commercial PP separator, and the thickness of the coated layer was approximately 23.65 μm, as observed in the cross-sectional view (Figure 3c). Furthermore, the TEM and EDS mapping in Figure 3d–h confirm the presence of Nb, Ni, and N elements in the Ni_3N/Nb_4N_5 heterostructure, indicating the successful incorporation of these elements. As demonstrated in Figure 3i, high-resolution TEM analysis clearly identified two characteristic interplanar distances measuring 0.250 nm and 0.203 nm, respectively. These were indexed to the (211) crystallographic plane of Nb_4N_5 and the (111) plane of Ni_3N, thus confirming the coexistence of both nitride phases. Additionally, a lattice spacing of 0.215 nm was observed, which corresponds to the (002) plane present in both Ni_3N and Nb_4N_5. These findings are consistent with the reference data for Nb_4N_5 (JCPDS No. 74-0606) and Ni_3N (JCPDS No. 89-5144) at 42° in the XRD spectra. Therefore, the Ni_3N/Nb_4N_5 heterostructure was successfully synthesized through the nitridation of $NiNb_2O_6$.

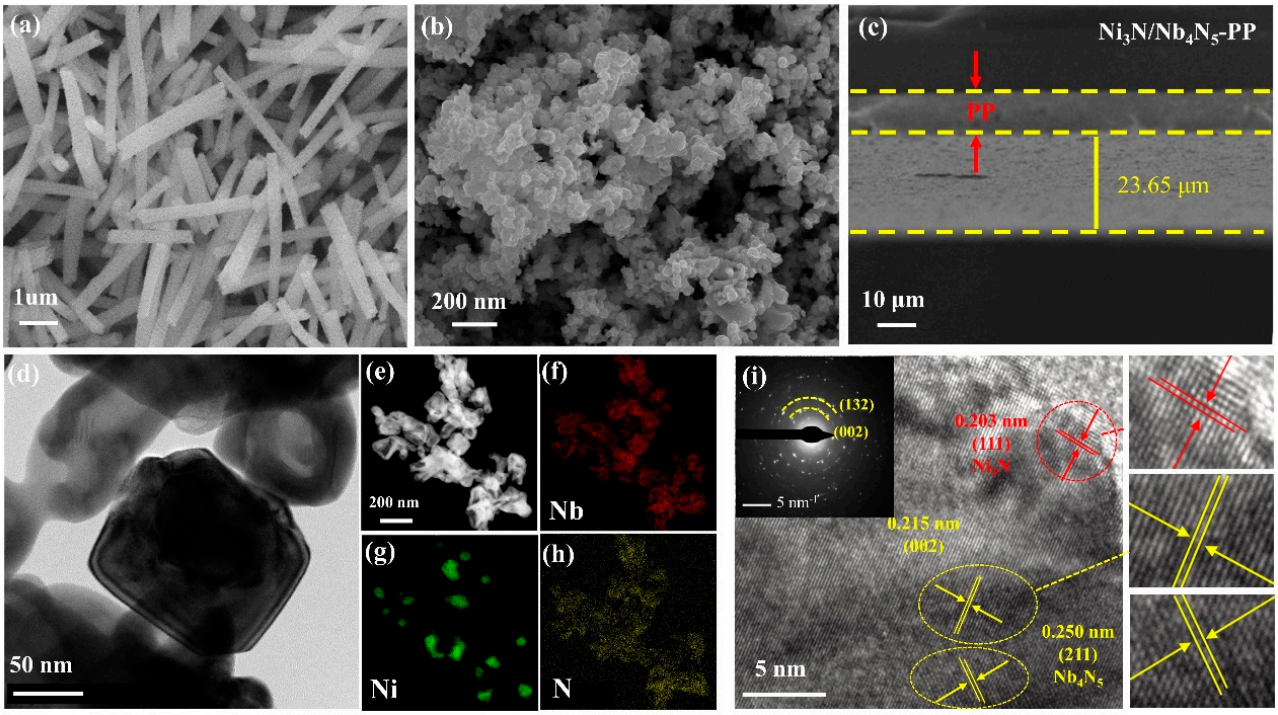


Figure 3. SEM image of (**a**) $NiNb_2O_6$ and (**b**) Ni_3N/Nb_4N_5 heterostructure; (**c**) cross-sectional SEM of Ni_3N/Nb_4N_5-PP; (**d**) low-magnification TEM image of Ni_3N/Nb_4N; (**e**–**h**) STEM image and EDS elemental mappings; (**i**) high-resolution TEM image of Ni_3N/Nb_4N.

In order to undertake a systematic investigation into the immobilization performance of LiPSs of the Ni_3N/Nb_4N_5 composite, comparative visual adsorption experiments were performed under controlled conditions. The quantitative results were then documented visually, as illustrated in Figure 4a–c. After 12 h of standing, the yellow color of the Li_2S_6 solution containing Ni_3N/Nb_4N_5 powder partially faded, whereas the solution with $NiNb_2O_6$ powder exhibited almost no color change. After 24 h, the yellow color of the Li_2S_6 solution with Ni_3N/Nb_4N_5 powder completely disappeared, while the solution containing $NiNb_2O_6$ showed only slight fading [47,48]. These results demonstrate that Ni_3N/Nb_4N_5 exhibits a significantly stronger adsorption capability for LiPSs compared to $NiNb_2O_6$.

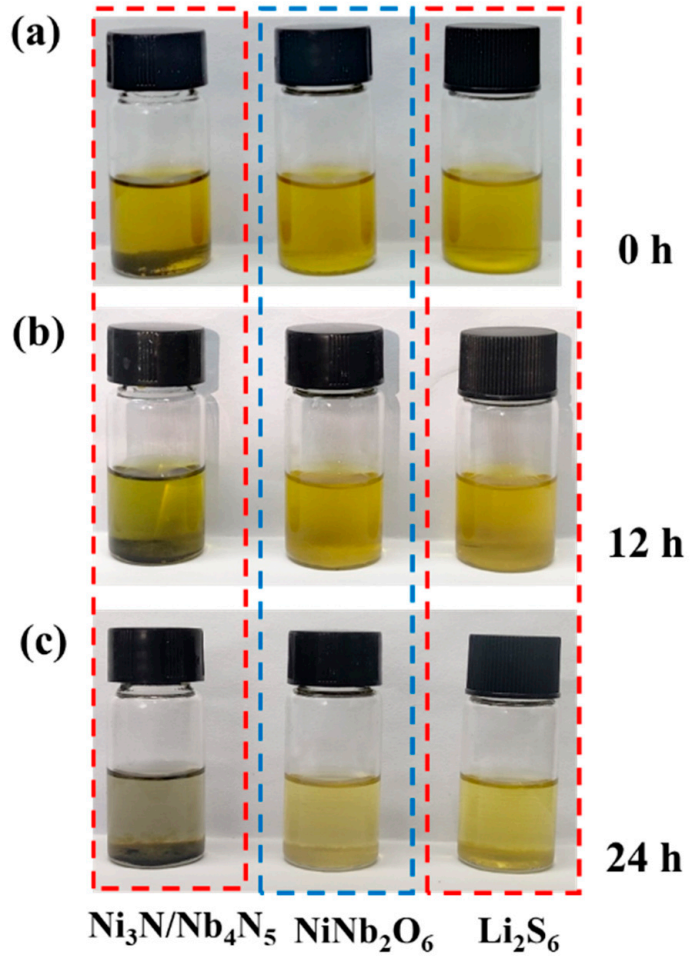


Figure 4. (**a**–**c**) Visual adsorption experiment of Li_2S_6 by pristine Ni_3N/Nb_4N_5 and $NiNb_2O_6$.

To further investigate the interaction mechanism between Ni_3N/Nb_4N_5 and LiPSs, XPS analysis was conducted on the samples before and after Li_2S_6 adsorption. Figure 5 presents the high-resolution XPS spectra of N 1s, Nb 3d, and Ni 2p before and after Li_2S_6 adsorption by Ni_3N/Nb_4N_5. In Figure 5a,d, the N 1s spectra exhibit three characteristic peaks corresponding to the Ni-N bond, Nb-N bond, and graphitic nitrogen. Following the adsorption of Li_2S_6, a shift in the peak positions of the three characteristic peaks was observed. The original peak positions of 397.03 eV/396.14 eV/398.84 eV shifted to higher binding energies of 0.11 eV, 0.31 eV, and 0.22 eV, respectively. In Figure 5b–e, the Nb 3d spectra display three pairs of characteristic peaks, assigned to Nb-O, Nb-N-O, and Nb-N bonds. The oxygen signal likely originates from surface oxidation due to exposure to air [37]. After the adsorption of Li_2S_6, the binding energies of Nb-O and Nb-N showed negligible changes; however, the Nb-N-O binding energy shifted to the right by 0.32 eV from the original 208.18 eV/205.38 eV. Previous studies have demonstrated that surface oxide layers on metal compounds can activate surface metal sites through strong chemical bonds for polysulfide bonding [49]. Similarly, the Ni 2p spectra (Figure 5c,f) show three pairs of characteristic peaks, including satellite peaks, Ni-O bonds, and Ni-N bonds. After Li_2S_6 adsorption, the binding energies of the Ni-O and Ni-N bonds increased by 0.45 eV and 0.29 eV, respectively.

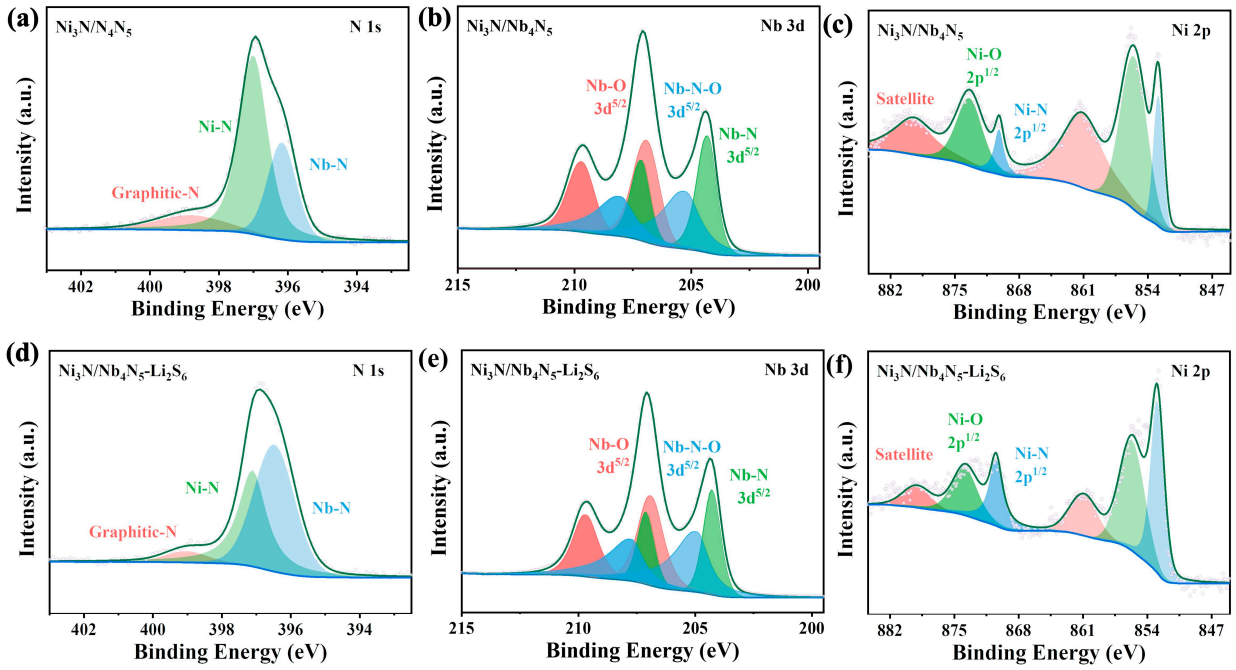


Figure 5. High-resolution XPS spectra of (**a**) N 1s, (**b**) Nb 3d, and (**c**) Ni 2p before Ni_3N/Nb_4N_5 adsorption of Li_2S_6, and (**d**) N 1s, (**e**) Nb 3d, and (**f**) Ni 2p after Ni_3N/Nb_4N_5 adsorption of Li_2S_6.

Compared to the Ni_3N/Nb_4N_5 heterostructure, the XPS high-resolution spectra of Nb 3d, O 1s [50,51], and Ni 2p [52,53] before/after the $NiNb_2O_6$ adsorption of Li_2S_6 are shown in Figure 6. No significant change in binding energy was observed before and after adsorption, indicating that Ni_3N/Nb_4N_5 exhibited stronger chemical adsorption capability for lithium LiPSs. This enhanced adsorption effectively suppressed the shuttle effect in Li-S batteries and improved the utilization of sulfur.

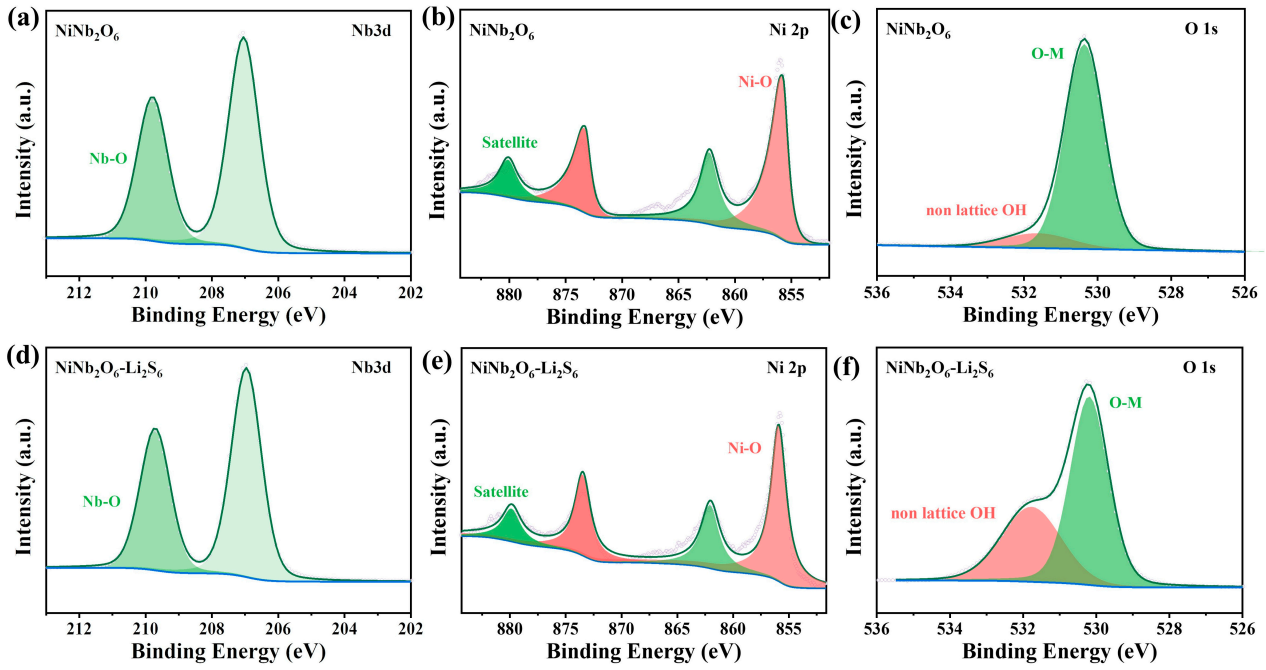


Figure 6. High-resolution XPS spectra of (**a**) Nb 3d, (**b**) Ni 2p, and (**c**) O 1s before $NiNb_2O_6$ adsorption of Li_2S_6, and high-resolution XPS spectra of (**d**) Nb 3d, (**e**) Ni 2p, and (**f**) O 1s after $NiNb_2O_6$ adsorption of Li_2S_6.

In addition, the high-resolution S 2p spectra of both Ni_3N/Nb_4N_5 and $NiNb_2O_6$ (Figure 7a,b) exhibit three pairs of characteristic peaks. The binding energy of terminal sulfur S_T^{-1} in Ni_3N/Nb_4N_5 (162.00 eV) was slightly higher than that in $NiNb_2O_6$ (161.94 eV). Similarly, the binding energy of bridging sulfur (S_B^0) in Ni_3N/Nb_4N_5 (163.70 eV) was higher than that in $NiNb_2O_6$ (163.63 eV). Additionally, the peak observed at 169.02 eV for Ni_3N/Nb_4N_5 can be assigned to thiosulfate species [54]. Compared with $NiNb_2O_6$, strong thiosulfate signals were detected in Ni_3N/Nb_4N_5, which could promote the conversion of higher-order LiPSs into short-chain lithium sulfides. This further demonstrates that Ni_3N/Nb_4N_5 plays a critical role in enhancing the kinetics of sulfide conversion, whereas only weak thiosulfate signals were observed in $NiNb_2O_6$ [55]. As demonstrated by visual adsorption tests and XPS characterization, the heterogeneous interface of Ni_3N/Nb_4N_5 facilitates charge transfer and exhibits enhanced thiophilicity, which promotes the adsorption of lithium LiPSs and effectively suppresses the shuttle effect in Li-S batteries.

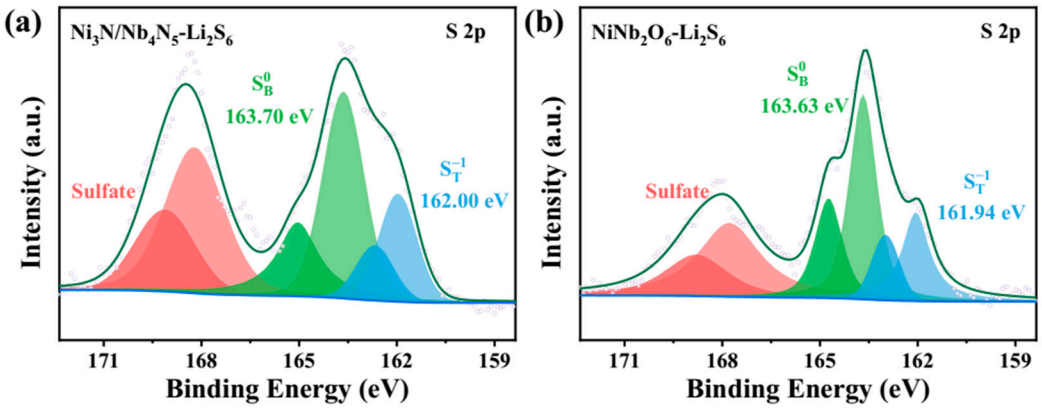


Figure 7. High-resolution XPS spectra of S 2p after adsorption of Li_2S_6 by (**a**) Ni_3N/Nb_4N_5 heterojunction and (**b**) $NiNb_2O_6$.

To investigate the effect of the Ni_3N/Nb_4N_5-modified separator on the electrochemical performance of Li-S batteries, the samples were coated onto a commercial separator for modification and the Li-S cells were assembled for electrochemical testing. Figure 8a presents the cyclic voltammetry (CV) curves of symmetric cells with different electrodes at a scan rate of 5 mV s^{-1}. It can be observed that the Ni_3N/Nb_4N_5 electrode exhibits higher redox current peaks and smaller redox peak separation compared to the $NiNb_2O_6$ electrode, whereas the CV curve of the $NiNb_2O_6$ cell shows greater potential hysteresis. The initial cycle of CV tests conducted at a scan rate of 0.1 mV s^{-1} for the Li-S cells assembled with Ni_3N/Nb_4N_5-PP, $NiNb_2O_6$-PP, and PP separators are shown in Figure 8b. The two reduction peaks observed at approximately 2.27 V and 1.97 V correspond to the conversion of S_8 to long-chain LiPSs and to the final products Li_2S_2/Li_2S, respectively. Additionally, the anodic peaks around 2.36 V and 2.48 V correspond to the conversion of Li_2S_2/Li_2S to long-chain LiPSs and S_8. The Ni_3N/Nb_4N_5-PP separator exhibits three distinct electrochemical advantages in comparison to both $NiNb_2O_6$-PP and PP separators. The following observations were made: firstly, there was a shift in the reduction peaks toward higher potentials; secondly, there was a decrease in the overpotential gap; and thirdly, there was a shift in the oxidation peaks to lower potentials. This combination of effects led to significantly lower charge–discharge overpotentials. This electrochemical behavior indicates that the Ni_3N/Nb_4N_5 heterostructure effectively promotes LiPS redox kinetics [56]. In order to conduct a more in-depth investigation into the interfacial characteristics, we undertook electrochemical impedance spectroscopy (EIS) measurements. The objective of this was to ascertain the charge transfer resistance (Rct) between the electrode and the electrolyte. As illustrated in Figure 8c, the resulting Nyquist plots for all cell

configurations are presented. The results revealed that the Rct of the Ni_3N/Nb_4N_5-PP cell (45.09 Ω) was significantly lower than that of the $NiNb_2O_6$-PP (72.12 Ω) and PP (242.1 Ω) cells, suggesting that Ni_3N/Nb_4N_5 accelerates electron transfer and reaction kinetics at the electrode–electrolyte interface [57].

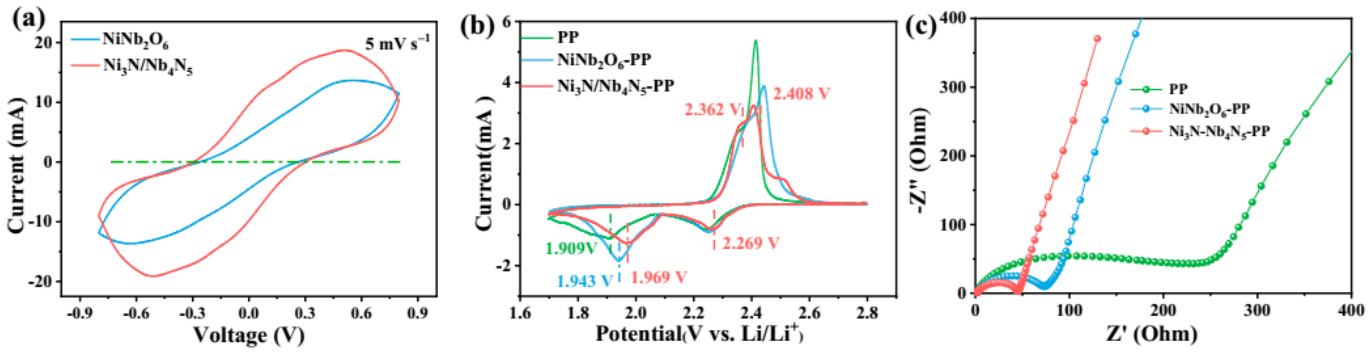


Figure 8. CV curves of (**a**) symmetric cells with Ni_3N/Nb_4N_5 and $NiNb_2O_6$; (**b**) the initial CV curve and (**c**) EIS curve of Li-S cells with Ni_3N/Nb_4N_5-PP, $NiNb_2O_6$-PP, and PP separators.

To investigate the capability of Ni_3N/Nb_4N_5 nanoparticles in catalyzing the conversion of LiPSs Li_2S, nucleation experiments were conducted. As illustrated in Figure 9a,b, the initial current drop is attributed to the reduction of higher-order LiPSs in the solution to Li_2S_4 [58]. The Ni_3N/Nb_4N_5 sample exhibited a significantly shorter nucleation time (4800 s) compared to $NiNb_2O_6$ (9300 s), indicating faster kinetics of Li_2S nucleation. Additionally, Ni_3N/Nb_4N_5 demonstrated a stronger Li_2S nucleation capability than $NiNb_2O_6$. This comparison suggests that the catalytic effect of Ni_3N/Nb_4N_5 can lower the energy barrier for Li_2S growth, thereby enhancing the conversion of soluble LiPSs to insoluble solid Li_2S [59].

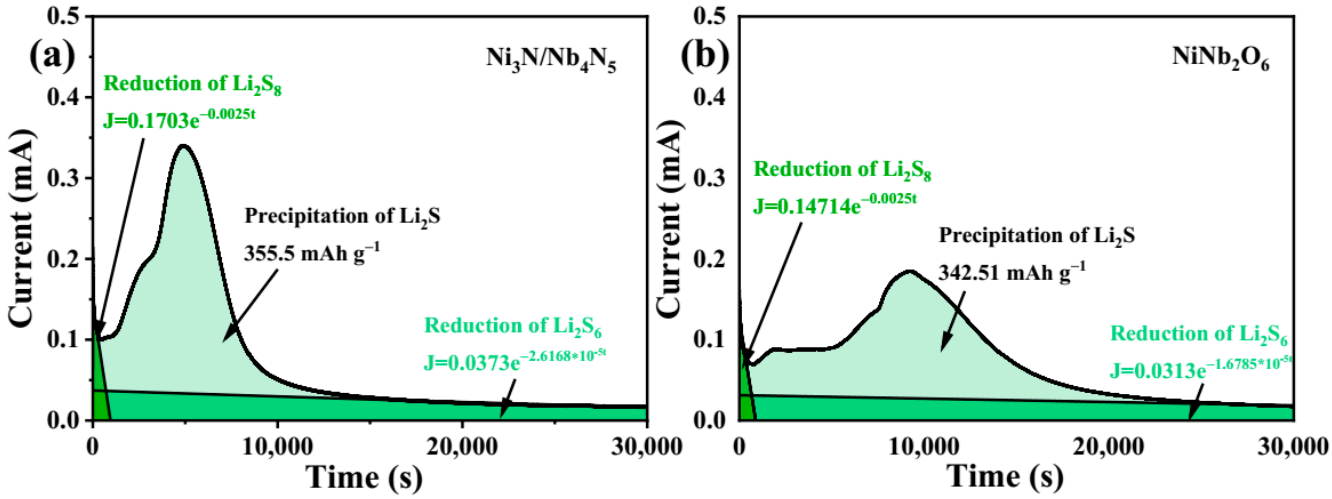


Figure 9. Potentiostatic discharge curves of (**a**) Ni_3N/Nb_4N_5 and (**b**) $NiNb_2O_6$ electrode.

Furthermore, the cycling stability of Li-S cells assembled with Ni_3N/Nb_4N_5-PP, $NiNb_2O_6$-PP, and PP separators was evaluated. The materials under consideration were Ni_3N/Nb_4N_5-PP, $NiNb_2O_6$-PP, and standard PP. Initial cycling tests conducted at 0.1 C rate revealed substantial differences in discharge capacities, with the Ni_3N/Nb_4N_5-PP -PP cell achieving 1403.6 mAh g^{-1}, outperforming both the $NiNb_2O_6$-PP (1224 mAh g^{-1}) and unmodified PP (948.6 mAh g^{-1}) counterparts. The corresponding charge–discharge profiles for the initial three cycles are illustrated in Figure 10a–c. It is important to note the observed potential difference at 800 mAh g^{-1} capacity, where the Ni_3N/Nb_4N_5-PP

system exhibited a minimal 0.17 V polarization, which is substantially lower than the 0.2 V and 0.24 V values recorded for the $NiNb_2O_6$-PP and PP systems, respectively. The reduced polarization suggests that the electrocatalytic activity of Ni_3N/Nb_4N_5 decreases the kinetic resistance of Li-S batteries, with Li-S cells with Ni_3N/Nb_4N_5-PP demonstrating low polarization and superior reversibility [14]. From the long-term cycling performance depicted in Figure 10d, it is evident that the Li-S cell with Ni_3N/Nb_4N_5-PP exhibited an initial discharge capacity of 1294.4 mAh g^{-1} at 0.2 C, and after 150 cycles, the discharge capacity was retained at 796.2 mAh g^{-1}, with a capacity decay rate of 0.25% per cycle. Electrochemical performance comparisons revealed significant differences among the tested separators. The $NiNb_2O_6$-PP configuration demonstrated an initial discharge capacity of 1011.9 mAh g^{-1}, which is considerably lower than that of the Ni_3N/Nb_4N_5-PP system. This observation serves to confirm the enhanced cycling stability of the latter. This performance discrepancy may originate from the inferior conductivity of $NiNb_2O_6$, as reported in previous studies [60,61]. It has been demonstrated that the Ni_3N/Nb_4N_5-PP cells exhibit superior cycling stability. This can be attributed to the formation of heterostructured interfaces, which enhance electron transport kinetics and reduce polarization loss during cycling. Furthermore, the high electrical conductivity of Ni_3N promotes the formation of a more homogeneous SEI layer, which inhibits the continuous decomposition of the electrolyte [62]. Testing the rate capability of the material across the range of 0.1–1.5 C (Figure 10e) demonstrated the exceptional performance of the Ni_3N/Nb_4N_5-PP, with capacities of 1403.6 mAh g^{-1} (0.1 C), 1032.4 mAh g^{-1} (0.25 C), 909.5 mAh g^{-1} (0.5 C), and 793.9 mAh g^{-1} (1.0 C) being maintained. It is noteworthy that even at the maximum 1.5 C rate, this system demonstrated a capacity of 695.4 mAh g^{-1}, which surpassed the capacities of both $NiNb_2O_6$-PP (634.5 mAh g^{-1}) and PP (235.7 mAh g^{-1}) systems. Upon returning to 0.1 C, the Ni_3N/Nb_4N_5-PP cell exhibited a recovery of 949.4 mAh g^{-1}, thereby further substantiating its superior rate adaptability and capacity retention in comparison to alternative configurations.

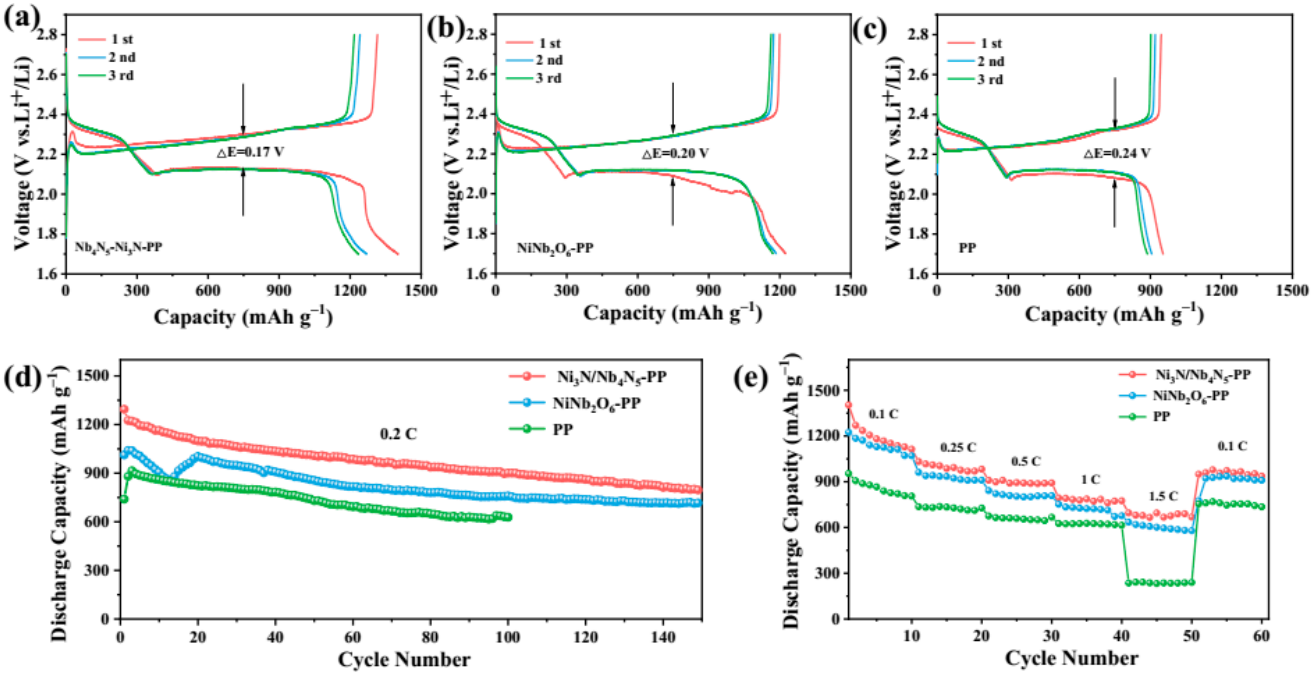


Figure 10. Charge–discharge curves of the first three cycles of Li-S cells with (**a**) Ni_3N/Nb_4N_5-PP, (**b**) $NiNb_2O_6$-PP, and (**c**) PP at 0.1 C; (**d**) cyclic performance of Li-S cells with Ni_3N/Nb_4N_5-PP, $NiNb_2O_6$-PP, and PP at 0.2 C; (**e**) rate performance.

4. Conclusions

In this study, the Ni_3N/Nb_4N_5 heterostructure was synthesized using electrospinning followed by nitridation treatment and applied as a modified separator for Li-S batteries. The Ni_3N/Nb_4N_5 heterostructure was uniformly dispersed and possessed abundant porosity, which facilitated ion transport. The visual adsorption tests and XPS results demonstrated that the Ni_3N/Nb_4N_5 had a strong adsorption capability for LiPSs, and the heterointerface promoted accelerated charge transfer. The Li_2S nucleation tests confirmed that the Ni_3N/Nb_4N_5 enhanced the nucleation and growth of Li_2S. The electrochemical measurements revealed that the Li-S cell with Ni_3N/Nb_4N_5-PP could deliver an initial discharge capacity of 1294.4 mAh g^{-1} at 0.2 C, with a capacity decay rate of 0.25% per cycle after 150 cycles, demonstrating superior cycling stability and rate performance compared to the Li-S cells with $NiNb_2O_6$-PP and pristine separator. This study introduces a novel method for fabricating the Ni_3N/Nb_4N_5 heterostructure, which markedly enhances the electrochemical performance of Li-S batteries.

Author Contributions: X.L.: writing—original draft preparation, writing—review and editing. W.S.: validation. S.Z.: writing—original draft preparation, data collection. C.X.: conceptualization, supervision. J.L.: project administration, writing—review and editing. G.L.: resources, supervision, funding acquisition. All authors have read and agreed to the published version of the manuscript.

Funding: This work was financially supported by the Natural Science Foundation of Guangdong Province (2023A1515010894), the Science and Technology Plan Project of Luzhou (2024RCX211), the PhD Innovation Studio and Special Research Project of Sichuan Vocational College of Chemical Technology (SCHYCXGZS-2024-02/YJKT2025040305), the Development Project for Metal Ion Removal from Wastewater Using Microreactors, and the research project cooperated with Jiangyin Longjicheng Pipe Jacking Engineering Co., Ltd.

Data Availability Statement: The data that support the findings of this study are available from the corresponding author upon reasonable request.

Conflicts of Interest: The authors declare no competing financial interests.

References

1. Li, Y.; Lu, J. Metal–air batteries: Will they be the future electrochemical energy storage device of choice. *ACS Energy Lett.* **2017**, *2*, 1370–1377. [CrossRef]
2. Jiang, L.; Luo, X.; Wang, D.W. A review on system and materials for aqueous flexible metal–air batteries. *Carbon Energy* **2023**, *5*, e284. [CrossRef]
3. Yaqoob, L.; Noor, T.; Iqbal, N. An overview of metal-air batteries, current progress, and future perspectives. *J. Energy Storage* **2022**, *56*, 106075. [CrossRef]
4. Ahmed, S.; Ali, A.; Asif, M.; Shim, J.; Park, G. Exploring innovative trends and advancements in rechargeable zinc-air batteries. *Inorg. Chem. Commun.* **2024**, *170*, 113288. [CrossRef]
5. Zhang, C.; Biendicho, J.J.; Zhang, T.; Du, R.; Li, J.; Yang, X.; Arbiol, J.; Zhou, Y.; Morante, J.R.; Cabot, A. Combined high catalytic activity and efficient polar tubular nanostructure in urchin-like metallic $NiCo_2Se_4$ for high-performance lithium–sulfur batteries. *Adv. Funct. Mater.* **2019**, *29*, 1903842.
6. Peng, H.; Huang, J.; Cheng, X.; Zhang, Q. Review on High-Loading and High-Energy Lithium–Sulfur Batteries. *Adv. Energy Mater.* **2017**, *7*, 1700260. [CrossRef]
7. Zhao, Y.; Wu, W.; Li, J.; Xu, Z.; Guan, L. Encapsulating MWNTs into hollow porous carbon nanotubes: A tube-in-tube carbon nanostructure for high-performance lithium-sulfur batteries. *Adv. Mater.* **2014**, *26*, 5113–5118. [CrossRef]
8. Kim, S.C.; Gao, X.; Liao, S.L.; Su, H.; Chen, Y.; Zhang, W.; Greenburg, L.; Pan, J.; Zheng, X.; Ye, Y.; et al. Solvation-property relationship of lithium-sulphur battery electrolytes. *Nat. Commun.* **2024**, *15*, 1268. [CrossRef]
9. Guo, D.; Yuan, M.; Zheng, X.; Li, M.; Nan, C.; Sun, G.; Huang, X.; Li, H. Ultralong cycle life enabled by in situ growth of $CoMo_{1-x}P$/Mo heterostructure for lithium-sulfur batteries. *J. Energy Chem.* **2022**, *73*, 5–12. [CrossRef]
10. Preefer, M.B.; Oschmann, B.; Hawker, C.J.; Seshadri, R.; Wudi, F. High sulfur content material with stable cycling in lithium-sulfur batteries. *Angew. Chem. Int. Ed.* **2017**, *129*, 15314–15318. [CrossRef]

11. Wang, Y.; Zhang, R.; Chen, J.; Wu, H.; Lu, S.; Wang, K.; Li, H.; Harris, C.J.; Xi, K.; Kumar, R.V.; et al. Enhancing catalytic activity of titanium oxide in lithium-sulfur batteries by band engineering. *Adv. Energy Mater.* **2019**, *9*, 1900953. [CrossRef]
12. Du, M.; Geng, P.; Pei, C.; Jiang, X.; Shan, Y.; Hu, W.; Ni, L.; Pang, H. High-entropy Prussian blue analogues and their oxide family as sulfur hosts for lithium-sulfur batteries. *Angew. Chem. Int. Ed.* **2022**, *61*, e202209350. [CrossRef] [PubMed]
13. Razzaq, A.A.; Yuan, X.; Chen, Y.; Hu, J.; Mu, Q.; Ma, Y.; Zhao, X.; Miao, L.; Ahn, J.H.; Peng, Y.; et al. Anchoring MOF-derived CoS_2 on sulfurized polyacrylonitrile nanofibers for high areal capacity lithium-sulfur batteries. *J. Mater. Chem. A* **2020**, *8*, 1298–1306. [CrossRef]
14. Shen, Z.; Zhang, Z.; Li, M.; Yuan, Y.; Zhao, Y.; Zhang, S.; Zhong, C.; Zhu, J.; Lu, J.; Zhang, H. Rational design of a $Ni_3N_{0.85}$ electrocatalyst to accelerate polysulfide conversion in lithium-sulfur batteries. *ACS Nano* **2020**, *14*, 6673–6682. [CrossRef] [PubMed]
15. Wang, R.; Jiao, J.; Liu, D.; He, Y.; Yang, Y.; Sun, D.; Pan, H.; Fnag, F.; Wu, R. High-entropy metal nitride embedded in concave porous carbon enabling polysulfide conversion in lithium-sulfur batteries. *Small* **2024**, *20*, 2405148. [CrossRef] [PubMed]
16. Cheong, J.L.; Hu, C.; Liu, W.; Ng, M.F.; Sullivan, M.B.; Ying, J.Y. 3D carbonaceous nanostructured transition metal nitride, carbonitride and carbide as polysulfide regulators for lithium-sulfur batteries. *Nano Energy* **2022**, *102*, 107659. [CrossRef]
17. Liu, R.; Liu, Z.; Liu, W.; Liu, Y.; Lin, X.; Li, Y.; Li, P.; Huang, Z.; Feng, X.; Yu, L.; et al. TiO_2 and Co nanoparticle-decorated carbon polyhedra as efficient sulfur host for high-performance lithium-sulfur batteries. *Small* **2019**, *15*, 1804533. [CrossRef]
18. Liu, Y.; Chatterjee, A.; Rusch, P.; Wu, C.; Nan, P.; Peng, M.; Bettels, F.; Li, T.; Ma, C.; Zhang, C.; et al. Monodisperse molybdenum nanoparticles as highly efficient electrocatalysts for Li-S batteries. *ACS Nano* **2021**, *15*, 15047–15056. [CrossRef]
19. Cai, D.; Liu, B.; Zhu, D.; Chen, D.; Lu, M.; Cao, J.; Wang, Y.; Huang, W.; Shao, Y.; Tu, H.; et al. Ultrafine Co_3Se_4 nanoparticles in nitrogen-doped 3D carbon matrix for high-stable and long-cycle-life lithium sulfur batteries. *Adv. Energy Mater.* **2020**, *10*, 1904273. [CrossRef]
20. Zhang, D.; Wang, S.; Hu, R.; Gu, J.; Cui, Y.; Li, B.; Chen, W.; Liu, C.; Shang, J.; Yang, S. Catalytic conversion of polysulfides on single atom zinc implanted MXene toward high-rate lithium-sulfur batteries. *Adv. Funct. Mater.* **2020**, *30*, 2002471. [CrossRef]
21. Liu, K.; Wang, X.; Gu, S.; Yuan, H.; Jiang, F.; Li, Y.; Tan, W.; Long, Q.; Chen, J.; Xu, Z.; et al. N, S-coordinated Co single atomic catalyst boosting adsorption and conversion of lithium polysulfides for lithium-sulfur batteries. *Small* **2022**, *18*, 2204707. [CrossRef]
22. Zhou, X.; Meng, R.; Zhong, N.; Yin, S.; Ma, G.; Liang, X. Size-dependent cobalt catalyst for lithium sulfur batteries: From single atoms to nanoclusters and nanoparticles. *Small Methods* **2021**, *5*, 2100571. [CrossRef] [PubMed]
23. Zhang, J.; Li, Z.; Fu, Q.; Xue, Y.; Cui, Z. The size-dependence of electrochemical thermodynamics of metal nanoparticles electrodes in theory and experiment. *J. Electrochem. Soc.* **2017**, *164*, 828–835. [CrossRef]
24. Zhang, L.; Chen, X.; Wan, F.; Niu, Z.; Wang, Y.; Zhang, Q.; Chen, J. Enhanced electrochemical kinetics and polysulfide traps of indium nitride for highly stable lithium-sulfur batteries. *ACS Nano* **2018**, *12*, 9578–9586. [CrossRef] [PubMed]
25. Luo, D.; Zhang, Z.; Li, G.; Cheng, S.; Li, S.; Li, J.; Gao, R.; Li, M.; Sy, S.; Deng, Y.; et al. Revealing the rapid electrocatalytic behavior of ultrafine amorphous defective Nb_2O_{5-x} nanocluster toward superior Li-S performance. *ACS Nano* **2020**, *14*, 4849–4860. [CrossRef] [PubMed]
26. Sun, T.; Zhao, X.; Li, B.; Shu, H.; Luo, L.; Xia, W.; Chen, M.; Zeng, P.; Yang, X.; Gao, P.; et al. $NiMoO_4$ nanosheets anchored on N-S doped carbon clothes with hierarchical structure as a bidirectional catalyst toward accelerating polysulfides conversion for Li-S Battery. *Adv. Funct. Mater.* **2021**, *31*, 2101285. [CrossRef]
27. Tian, D.; Song, X.; Wang, M.; Wu, X.; Qiu, Y.; Guan, B.; Xu, X.; Fang, L.; Zhang, N.; Sun, K. MoN supported on graphene as a bifunctional interlayer for advanced Li-S batteries. *Adv. Energy Mater.* **2019**, *9*, 1901940. [CrossRef]
28. Zhang, H.Y.; Dai, R.Q.; Zhu, S.; Zhou, L.Z.; Xu, Q.J.; Min, Y.L. Bimetallic nitride modified separator constructs internal electric field for high-performance lithium-sulfur battery. *Chem. Eng. J.* **2022**, *429*, 132454. [CrossRef]
29. Yan, Y.; Li, H.; Cheng, C.; Yan, T.; Gao, W.; Mao, J.; Dai, K.; Zhang, L. Boosting polysulfide redox conversion of Li-S batteries by one-step-synthesized Co-Mo bimetallic nitride. *J. Energy Chem.* **2021**, *61*, 336–346. [CrossRef]
30. He, J.R.; Chen, Y.F.; Manthiram, A. Vertical Co_9S_8 hollow nanowall arrays grown on a Celgard separator as a multifunctional polysulfide barrier for high-performance Li-S batteries. *Energy Environ. Sci.* **2018**, *11*, 2560–2568. [CrossRef]
31. Sun, L.; Liu, Y.; Xie, J.; Fan, L.; Wu, J.; Jiang, R.; Jin, Z. Polar Co_9S_8 anchored on pyrrole-modified graphene with in situ growth of CNTs as multifunctional self-supporting medium for efficient lithium-sulfur batteries. *Chem. Eng. J.* **2023**, *451*, 138370. [CrossRef]
32. Wang, D.; Guo, Q.; Hong, X.; Xie, K.; Ma, Z.; Zheng, C.; Xiong, S. Monodispersed FeS_2 electrocatalyst anchored to nitrogen-doped carbon host for lithium-sulfur batteries. *Adv. Funct. Mater.* **2022**, *32*, 2205471.
33. Jiang, X.; Zhang, S.; Zou, B.; Li, G.; Yang, S.; Zhao, Y.; Lian, J.; Li, H.; Ji, H. Electrospun CoSe@ NC nanofiber membrane as an effective polysulfides adsorption-catalysis interlayer for Li-S batteries. *Chem. Eng. J.* **2022**, *430*, 131911. [CrossRef]
34. Zhao, M.; Chen, X.; Li, X.Y.; Li, B.Q.; Huang, J.Q. Lithium-sulfur batteries: An organodiselenide comediator to facilitate sulfur redox kinetics in lithium-sulfur batteries. *Adv. Mater.* **2021**, *33*, 2170100. [CrossRef]

35. Wang, X.; Zhang, L.; Zhang, C.; Ma, X.; Jin, Q.; Li, L.; Zhang, Z.; Zhang, X.; Wu, L. Strengthened dipole-dipole interaction on high-entropy oxide electrocatalysts for high-rate and excellently stable lithium-sulfur batteries. *J. Energy Chem.* **2025**, *105*, 292–301. [CrossRef]
36. Rai, A.K.; Anh, L.T.; Gim, J.; Mathew, V.; Kang, J.; Paul, B.J.; Song, J.; Kim, J. Simple synthesis and particle size effects of TiO_2 nanoparticle anodes for rechargeable lithium ion batteries. *Electrochim. Acta* **2013**, *90*, 112–118. [CrossRef]
37. Jung, S.K.; Hwang, I.; Chang, D.; Park, K.Y.; Kim, S.J.; Seong, W.M.; Eum, D.; Park, J.; Kim, B.; Kim, J.; et al. Nanoscale phenomena in lithium-ion batteries. *Chem. Rev.* **2020**, *120*, 6684–6737. [CrossRef]
38. Li, Y.; Qian, J.; Zhang, M.; Wang, S.; Wang, Z.; Li, M.; Bai, Y.; An, Q.; Xu, H.; Wu, F.; et al. Co-construction of sulfur vacancies and heterojunctions in tungsten disulfide to induce fast electronic/ionic diffusion kinetics for sodium-ion batteries. *Adv. Mater.* **2020**, *32*, e2005802. [CrossRef]
39. Li, B.; Su, Q.; Yu, L.; Zhang, J.; Du, G.; Wang, D.; Han, D.; Zhang, M.; Ding, S.; Xu, B. Tuning the band structure of MoS_2 via Co_9S_8@MoS_2 core-shell structure to boost catalytic activity for lithium-sulfur batteries. *ACS Nano* **2020**, *14*, 17285–17294. [CrossRef]
40. Zhou, T.; Lv, W.; Li, J.; Zhou, G.; Zhao, Y.; Fan, S.; Liu, B.; Li, B.; Kang, F.; Yang, Q.H. Twinborn TiO_2-TiN heterostructures enabling smooth trapping-diffusion-conversion of polysulfides towards ultralong life lithium-sulfur batteries. *Energy Environ. Sci.* **2017**, *10*, 1694–1703. [CrossRef]
41. Ren, Y.; Zhai, Q.; Wang, B.; Hu, L.; Ma, Y.; Dai, Y.; Tang, S.; Meng, X. Synergistic adsorption-electrocatalysis of 2D/2D heterostructure toward high performance Li-S batteries. *Chem. Eng. J.* **2022**, *439*, 135535. [CrossRef]
42. Yao, W.; Zheng, W.; Xu, J.; Tian, C.; Han, K.; Sun, W.; Xiao, S. ZnS-SnS@NC heterostructure as robust lithiophilicity and sulfiphilicity mediator toward high-rate and long-life lithium-sulfur batteries. *ACS Nano* **2021**, *15*, 7114–7130. [CrossRef] [PubMed]
43. Lei, D.; Shang, W.; Zhang, X.; Li, Y.; Qiao, S.; Zhong, Y.; Deng, X.; Shi, X.; Zhang, Q.; Hao, C.; et al. Facile synthesis of heterostructured MoS_2-MoO_3 nanosheets with active electrocatalytic sites for high-performance lithium-sulfur batteries. *ACS Nano* **2021**, *15*, 20478–20488. [CrossRef] [PubMed]
44. Jamnik, J.; Maier, J. Nanocrystallinity effects in lithium battery materials Aspects of nano-ionics. *Phys. Chem. Chem. Phys.* **2003**, *5*, 5215–5220. [CrossRef]
45. Xu, Z.L.; Lin, S.; Onofrio, N.; Zhou, L.; Shi, F.; Lu, W.; Kang, K.; Zhang, Q.; Lau, S.P. Exceptional catalytic effects of black phosphorus quantum dots in shuttling-free lithium sulfur batteries. *Nat. Commun.* **2018**, *9*, 4164. [CrossRef]
46. Li, Z.; Ma, Z.; Wang, Y.; Chen, R.; Wu, Z.; Wang, S. LDHs derived nanoparticle-stacked metal nitride as interlayer for long-life lithium sulfur batteries. *Sci. Bull.* **2018**, *63*, 169–175. [CrossRef]
47. ABhargav, J.R.; He, A.; Gupta, A. Manthiram, Lithium-sulfur batteries: Attaining the critical metrics. *Joule* **2020**, *4*, 285–291. [CrossRef]
48. Lim, W.G.; Kim, S.; Jo, C.; Lee, J. A comprehensive review of materials with catalytic effects in Li-S batteries: Enhanced redox kinetics. *Angew. Chem. Int. Ed.* **2019**, *58*, 18746–18757. [CrossRef]
49. Fan, S.; Huang, S.; Pam, M.E.; Chen, S.; Wu, Q.; Hu, J.; Wang, Y.; Ang, L.K.; Yan, C.; Shi, Y.; et al. Design multifunctional catalytic interface: Toward regulation of polysulfide and Li. *Small* **2019**, *15*, e1906132. [CrossRef]
50. Tan, L.; Zhou, S.; Jin, Y.; Zhu, H.; Zhang, Q.; Guo, J.; Li, X.; Dong, Z.; Yang, N.; Cong, Y. Spontaneous electrochemical reconstruction of $NiNb_2O_6$@C for high-rate lithium-ion batteries. *Chem. Eng. J.* **2024**, *495*, 153397. [CrossRef]
51. Zhao, S.; Lian, J.; Zhang, S.; Cui, Y.; Li, G.; Wang, Y.; Li, H. Molten salt synthesis of submicron $NiNb_2O_6$ anode material with ultra-high rate performance for lithium-ion batteries. *Chem. Eng. J.* **2023**, *461*, 141997. [CrossRef]
52. Chen, H.; Cheng, H.; Liu, H.; Hu, Y.; Yuan, T.; Dai, S.; Liu, M.; Hu, H. Design of phase interface and defect in niobium-nickel oxide for ultrafast Li-ion storage. *J. Mater. Sci. Technol.* **2023**, *147*, 145–152. [CrossRef]
53. Bharti, B.; Kumar, S.; Lee, H.N.; Kumar, R. Formation of oxygen vacancies and Ti^{3+} state in TiO_2 thin film and enhanced optical properties by air plasma treatment. *Sci. Rep.* **2016**, *6*, 32355. [CrossRef]
54. He, M.; Li, X.; Li, W.; Zheng, M.; Wang, J.; Ma, S.; Yin, G.; Zuo, P.; Sun, X. Immobilization and kinetic promotion of polysulfides by molybdenum carbide in lithium-sulfur batteries. *Chem. Eng. J.* **2021**, *411*, 128563. [CrossRef]
55. Luo, Z.H.; Zheng, M.; Zhou, M.X.; Sheng, X.T.; Chen, X.L.; Shao, J.J.; Wang, T.S.; Zhou, G. 2D Nanochannel interlayer realizing high-performance lithium-sulfur batteries. *Adv. Mater.* **2025**, *37*, 2417321. [CrossRef] [PubMed]
56. Li, W.; Gong, Z.; Yan, X.; Wang, D.; Liu, J.; Guo, X.; Zhang, Z.; Li, G. In situ engineered ZnS-FeS heterostructure in N-doped carbon nanocages accelerating polysulfide redox kinetics for lithium sulfur batteries. *J. Mater. Chem. A* **2020**, *8*, 433–442. [CrossRef]
57. Chung, S.H.; Manthiram, A. A polyethylene glycol-supported microporous carbon coating as a polysulfide trap for utilizing pure sulfur cathodes in lithium-sulfur batteries. *Adv. Mater.* **2014**, *26*, 7352–7357. [CrossRef]
58. Fan, F.Y.; Carter, W.C.; Chiang, Y.M. Mechanism and kinetics of Li_2S precipitation in lithium-sulfur batteries. *Adv. Mater.* **2015**, *27*, 5203–5209. [CrossRef]

59. Kong, Z.; Lin, Y.; Hu, J.; Wang, Y.; Zhan, L. Phosphorus doped hierarchical porous carbon nanosheet array as an electrocatalyst to enhance polysulfides anchoring and conversion. *Chem. Eng. J.* **2022**, *436*, 132719. [CrossRef]
60. Huang, S.; Wang, Z.; Von Lim, Y.; Wang, Y.; Li, Y.; Zhang, D.; Yang, H.Y. Recent advances in heterostructure engineering for lithium-sulfur batteries. *Adv. Energy Mater.* **2021**, *11*, 2003689. [CrossRef]
61. Li, R.; Zhou, X.; Shen, H.; Yang, M.; Li, C. Conductive holey MoO_2-Mo_3N_2 heterojunctions as job-synergistic cathode host with low surface area for high-loading Li-S batteries. *ACS Nano* **2019**, *13*, 10049–10061. [CrossRef] [PubMed]
62. Liang, W.; Zhou, X.; Zhang, B.; Zhao, Z.; Song, X.; Chen, K.; Wang, L.; Ma, Z.; Liu, J. The versatile establishment of charge storage in polymer solid electrolyte with enhanced charge transfer for LiF-rich SEI generation in lithium metal batteries. *Angew. Chem.* **2024**, *136*, e202320149. [CrossRef]

Disclaimer/Publisher's Note: The statements, opinions and data contained in all publications are solely those of the individual author(s) and contributor(s) and not of MDPI and/or the editor(s). MDPI and/or the editor(s) disclaim responsibility for any injury to people or property resulting from any ideas, methods, instructions or products referred to in the content.